



Star-like, dopant-free, corannulene-cored hole transporting materials for efficient inverted perovskite solar cells

Ming-Wei An^{b,d,1}, Bolin Li^{b,1}, Bin-Wen Chen^d, Zuo-Chang Chen^d, Han-Rui Tian^d, Lin-Long Deng^{c,*}, Xugang Guo^b, Zhou Xing^{a,*}

^a Fujian Key Laboratory of Polymer Materials, Fujian Provincial Key Laboratory of Advanced Materials Oriented Chemical Engineering, College of Chemistry & Materials Science, Fujian Normal University, Fuzhou, Fujian 350007, China

^b Department of Materials Science and Engineering, Southern University of Science and Technology, Shenzhen 518055, China

^c Pen-Tung Sah Institute of Micro-Nano Science and Technology, Xiamen University, Xiamen 361005, China

^d State Key Lab for Physical Chemistry of Solid Surfaces, iChEM (Collaborative Innovation Center of Chemistry for Energy Materials), Department of Chemistry, College of Chemistry and Chemical Engineering, Xiamen University, Xiamen 361005, China

ARTICLE INFO

Keywords:

Perovskite solar cells
Corannulene
Hole transporting materials
Power conversion efficiency
Stability

ABSTRACT

Hole transporting materials (HTMs), owing to their unique bottom position in inverted perovskite solar cells (PSCs), exert a considerable influence on the hole-transporting process and the morphology/performance of the perovskite layers. Considering the well-known interfacial problems associated with commonly-used NiO_x and poly(triarylamine) HTMs in traditional inverted PSCs, there is an urgent need for exploring efficient HTMs exhibiting good film formability/processability and interfacial contact to meet the specific requirements of high-performance and stable inverted PSCs. Herein, we fabricated inverted PSCs involving two star-like, dopant-free, corannulene-cored HTMs with O-terminals (*sym*-penta(*N*, *N*-bis(4-methoxyphenyl)aniline)corannulene, namely Cor-OMePTPA) and S-terminals (*sym*-penta(*N*, *N*-bis(4-(methylthio)phenyl)aniline)corannulene, namely Cor-SMePTPA) for the first time. The Cor-SMePTPA HTM exhibited a stronger hole-transporting ability and a better interfacial chemical linkage when compared to the Cor-OMePTPA HTM. The device containing Cor-SMePTPA HTM delivered a power conversion efficiency of 21.70%, which was the highest among inverted PSCs based on methylthio (SMe)-terminated HTMs. Furthermore, comprehensive experimental and theoretical characterizations clearly showed that the core and outer terminals (O or S) affected the optoelectric and chemical properties of the HTMs as well as the photovoltaic performance and stability of the corresponding PSCs, highlighting the superiority of the design involving a corannulene core and SMe groups in HTMs for inverted PSCs. We believe that such dopant-free corannulene-cored HTMs can have considerable potential for realizing highly efficient and stable PSCs in the future.

1. Introduction

The power conversion efficiency (PCE) of inverted structure (*p-i-n*) perovskite solar cells (PSCs) has exceeded 25%, providing motivation for researchers to explore efficient functional materials for promoting device performance and stability. [1] Generally, the main architecture of PSCs comprises conductive glass substrates, hole transporting layers (HTLs), perovskite layers, electron transporting layers (ETLs) and electrodes. [2] Differed from the regular counterparts, the HTLs are the first layer to be deposited in inverted devices, indicating that HTLs are fabricated prior to perovskite and other functional layers. Accordingly,

as-prepared HTLs considerably determine the morphology and performance of upper layers, thus affecting device performance and stability. [3].

With a low raw material cost, an ideal energy level, and a good hole-transporting ability, NiO_x has been considered the most efficient inorganic HTL for state-of-the-art inverted PSCs. [4] However, it has been reported that the Ni^{≥3+} sites in NiO_x films play an undesirable role in deprotonating cationic amines and oxidizing the iodide species of perovskites, resulting in the decomposition of perovskite materials and the formation of Pb-rich hole extraction barriers at the NiO_x/perovskite interface, adversely affecting the long-term stability of devices. [5] Poly

* Corresponding authors.

E-mail addresses: denglinlong@xmu.edu.cn (L.-L. Deng), zhouxing@fjnu.edu.cn (Z. Xing).

¹ These authors contributed equally to this work.

(triarylamine) (PTAA), an even more widely known organic HTL, is currently the most commonly used polymeric HTL in high-performance inverted devices. [6] However, fabricating perfect perovskite films on the surface of untreated PTAA films is difficult because of the strong hydrophobicity of polymers, limiting the further application of PTAA HTLs in terms of large-area and tandem PSCs. [7] Recently, with desirable anchoring features and optoelectrical properties, self-assembled monolayers (SAMs) have emerged as an efficient HTL for perovskite photovoltaics that can increase the device PCE to over 20%. [3] There are ongoing studies on the molecular design and mechanism of SAM hole transporting materials (HTMs). To sum up, the critical influence of bottom HTLs on inverted device performance and stability shows that the targeted molecular design of the HTM structure is important for meeting the specific requirements for inverted PSCs (Fig. 1).

To solve the aforementioned problems of traditional HTLs, herein, we fabricated two star-like, dopant-free, corannulene-cored HTMs, *sym*-penta(*N*, *N*-bis(4-methoxyphenyl)aniline)corannulene (Cor-OMePTPA) and *sym*-penta(*N*, *N*-bis(4-(methylthio)phenyl)aniline)corannulene (Cor-SMePTPA), into inverted PSCs for the first time. The molecular structure of HTMs can be generally divided into two major parts: corannulene core and functional arms. The corannulene core differs from other planar organic cores in being able to decrease the tendency to spontaneous aggregation and the film hydrophobicity, contributing to excellent film formability/processability for the HTL and the upper perovskite layer. [8] Furthermore, the unique bowl shape of the corannulene core leads to a natural dipole moment and an ideal packing mode for the material [9], facilitating efficient charge transport. [10] On the other hand, the deliberately designed functional arms regulate energy levels and increase the hole mobility of the HTM, while playing a key role in enhancing the interfacial chemical linkage between the HTL and perovskite layer, contributing to the prevention of film delamination and interface destruction. Subsequently, we performed comprehensive theoretical and experimental characterizations to understand the effects of the core and the outer terminals on the molecular and film properties of the investigated HTMs. The performance and interfacial

problems of the device were improved by replacing the traditional methoxy (OMe) terminals in the corannulene-cored HTMs with stronger Lewis-base methylthio (SMe) terminals. This strategy endowed the Cor-SMePTPA-based inverted PSC with a PCE exceeding 21% and a light-soaking stability lifetime of ~1000 h. Notably, the PCE of 21.70% was the highest among inverted devices with SMe-terminated HTMs reported so far (Figs. 1 and S1). We believe that this work can offer specific guidance in designing novel HTMs for high-performance and stable inverted PSCs.

2. Results and discussions

The molecular structures and chemical properties of the two corannulene-cored HTMs investigated in this study are illustrated in Fig. 2. As shown in Fig. 2a, the molecular template had three design components: a corannulene core (the red region), triphenylamine (TPA) bridging moieties (the yellow region), and O/SMe outer terminals (the blue region). First, the polar corannulene core endowed the material with excellent solubility, [8,9] facilitating solution processing of the HTL and the perovskite layer. Second, the TPA moiety, one of the most efficient building blocks in state-of-the-art HTMs, ensured good hole-transporting ability for the materials. [6] Third, different terminals (OMe or SMe) outside the TPA moieties were deliberately designed to interact with the Pb species in perovskite to enhance the interfacial chemical linkage between the HTL and perovskite layer. [3] The synthetic route and nuclear magnetic resonance (NMR) data of Cor-OMePTPA were reported in our previous study, [9] and the synthesis details and $^1\text{H}/^{13}\text{C}$ NMR spectra of the novel Cor-SMePTPA material are listed in Fig. S2-4 of the Supplementary Information. Furthermore, we performed physical/chemical tests to explore the different molecular influences of Cor-SMePTPA and Cor-OMePTPA on the corresponding film properties, device performance and stability.

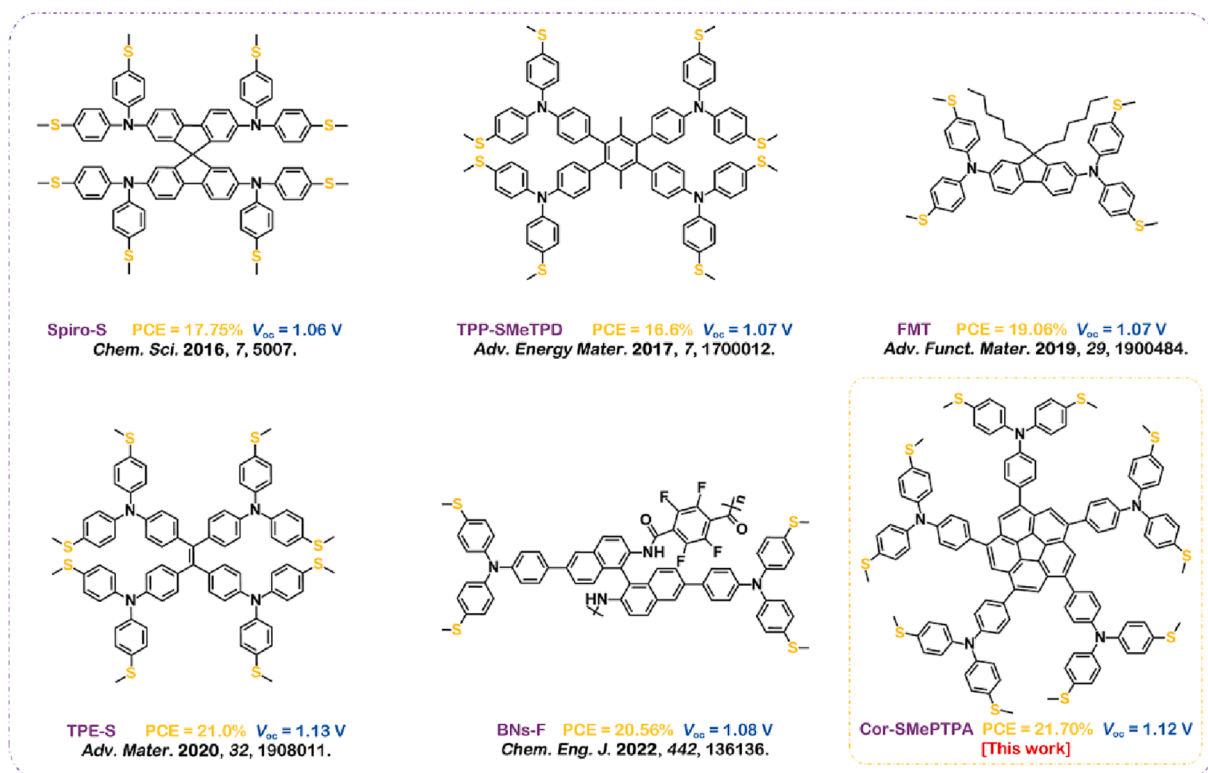


Fig. 1. Molecular structures of the representative SMe-terminated HTMs for efficient inverted PSCs and the comparison of PCE and V_{oc} between this work and them.

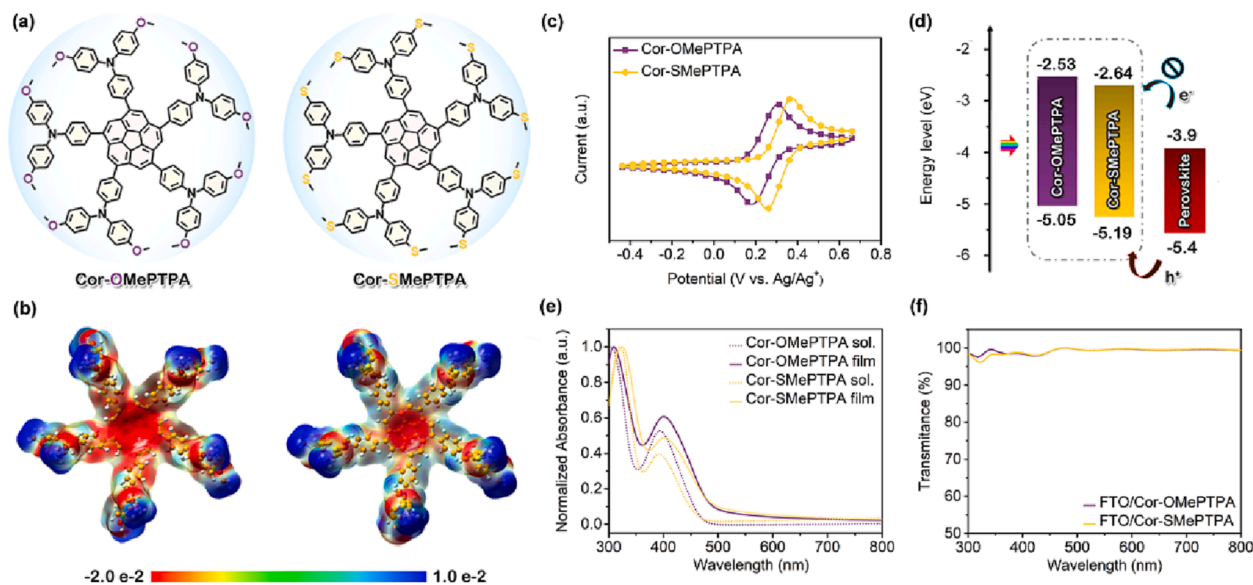


Fig. 2. (a) Molecular structures, (b) ESP simulation, (c) CV curves, (d) Energy levels, (e) UV–Vis absorption spectra and (f) Transmittance spectra of Cor-OMePTPA and Cor-SMePTPA (the baseline of substrate has been deducted), respectively.

2.1. Physical and chemical properties of the HTMs

First, we performed a density functional theory (DFT) simulation and cyclic voltammetry (CV) analysis to investigate the electronic properties of the two HTMs since the intrinsic natures of HTMs considerably affects the HTL properties of devices. [11] Fig. 2b shows the electrostatic potential (ESP) simulation of each molecule. The terminal atoms (O and S) were more positive than either corannulene cores or TPA groups. Besides, we found that compared to the O atom, the S atom has a more positive ESP and therefore is a stronger Lewis base that can interact with the Pb^{2+} species of perovskite more easily, [12,13] contributing to the passivation of Pb-related defects in perovskites. [14] In Fig. S5, an evident shift in the binding energy in the X-ray photoelectron spectroscopy (XPS) spectra for the Cor-SMePTPA-Perovskite sample compared to that for the Cor-OMePTPA-Perovskite sample is observed, confirming that the Pb-S interaction between perovskite and Cor-SMePTPA is stronger than the Pb-O interaction between perovskite and Cor-OMePTPA. Furthermore, we investigated the electrochemical properties of the two HTMs by performing CV tests, as shown in Fig. 2c. We observed that the CV curves were completely reversible, indicating ideal electrochemical stability for these two HTMs. Fig. 2d and Table S1 list the highest occupied molecular orbital (HOMO) values for Cor-SMePTPA and Cor-OMePTPA, which are well-matched with the valence band maximum of perovskite. [15] Specifically, the HOMO value of Cor-SMePTPA (-5.19 eV) was lower than that of Cor-OMePTPA (-5.05 eV) due to the replacement of OMe terminals with SMe terminals, which was calculated based on ultraviolet photoelectron spectroscopy (UPS) results shown in Fig. S6. The UV–Vis absorption spectra of the two HTMs obtained in solution and for the thin-film state are clearly depicted in Fig. 2e, and both exhibit two peaks at approximately 300 and 400 nm in the curves. The absorption curves of the films exhibited red shifts relative to those obtained in the solution state because of π - π packing of molecules. [16] According to the absorption spectra, we estimated that the bandgaps of Cor-SMePTPA and Cor-OMePTPA were 2.55 and 2.52 eV, respectively. Correspondingly, the lowest unoccupied molecular orbital (LUMO) values were calculated to be -2.64 and -2.53 eV, also proving the good electron-blocking ability of these HTMs (Fig. 2d), which in turn contributes to decrease charge recombination at the HTL/perovskite interface in the devices.

Second, since light entered the inverted PSC from the bottom of the HTL, the light absorption of the HTLs affected the absorbance of

perovskite films, and thus the photovoltaic performance of the devices. Fig. 2f is a comparison of the transmittances of the two HTM films deposited on fluorine-doped tin oxide (FTO) substrates for which the FTO baseline has been deducted. Fortunately, we found that both the targeted materials exhibited extremely high transmittances above 95% in the range of 300–800 nm, revealing that the deposition of these HTLs did not decrease the light absorbance of perovskite films in the devices.

Third, the bottom HTLs underwent several rounds of thermal annealing until the completion of device fabrication. Therefore, thermal stability is an important consideration for HTLs. As displayed in Fig. S7, we chose Cor-SMePTPA as a representative molecule to evaluate the thermal stability of the investigated corannulene-cored HTMs using thermogravimetric analysis (TGA). The TGA curve clearly confirmed the excellent thermal stability of the corannulene-cored HTM with a decomposition temperature above 390 °C, revealing that the material remained completely stable during the thermal annealing process. Based on the aforementioned favorable physical and chemical properties, it is reasonable to conclude that these two materials are suitable for fabricating HTM films for inverted devices.

2.2. Morphological properties of the HTM films

In this section, we focused on studying the relation between the morphological properties of different HTM films and the targeted perovskite layers above these films. Water contact angle tests were performed to evaluate surface hydrophilicity of different HTM films, as shown in Fig. 3a and 3b. Due to the high polarity of the corannulene core, surface wettability of the HTM films is sufficient for fabricating perovskite films above the HTLs. Furthermore, the water contact angle of the Cor-SMePTPA sample (83.4°) was slightly higher than that of the Cor-OMePTPA sample (70.9°), which might contribute to the larger grain size of perovskite on the Cor-SMePTPA HTLs. [17,18].

To verify our speculation, we recorded scanning electron microscopy (SEM) images of top and cross-sectional views of different perovskite films, as depicted in Fig. 3c–g and S8. Fig. 3c shows the surface morphology of FTO substrates, which can be regarded as the control sample. Then, we spin-coated Cor-SMePTPA and Cor-OMePTPA solutions onto the FTO substrates and annealed the resulting samples at 100 °C for 20 min to completely evaporate the solvents. Surprisingly, negligible morphological variations were observed after depositing the HTM films, according to Fig. 3d and 3e. We can rationalize this result in

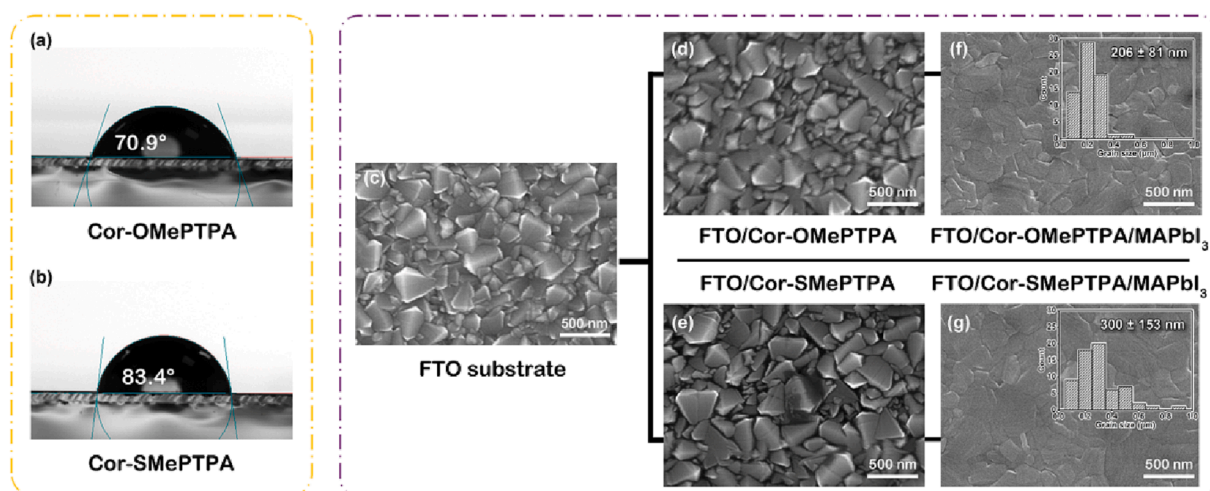


Fig. 3. Surface wettability tests of (a) Cor-OMePTPA and (b) Cor-SMePTPA films. Top-view SEM images of (c) FTO substrate, (d) FTO/Cor-OMePTPA, (e) FTO/Cor-SMePTPA, (f) FTO/Cor-OMePTPA/MAPbI₃ and (g) FTO/Cor-SMePTPA/MAPbI₃ samples, respectively. Insets are the statistic perovskite grain size of each samples.

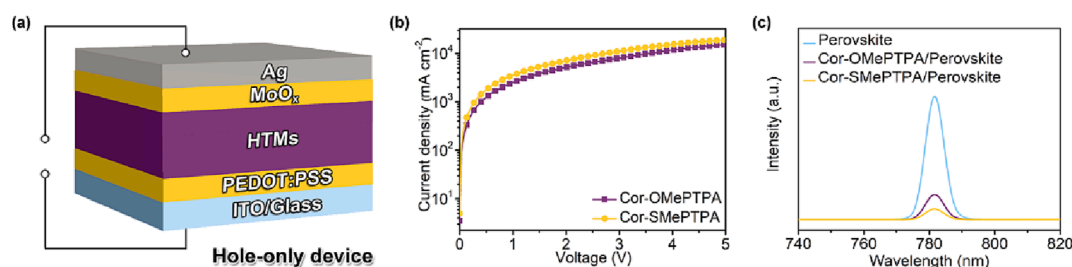


Fig. 4. (a) The architecture of hole-only device in this work. (b) *J*-*V* curves recorded in dark condition based on SCLC method and (c) PL spectra of different samples, respectively.

terms of the ultrathin and amorphous nature of the HTM films, which promotes interfacial contact and charge extraction. [17] Furthermore, we observed from spin-coating MAPbI₃ films above the HTM films, as shown in Fig. 3f and 3g, that the grain size of the Cor-SMePTPA/MAPbI₃ sample was larger compared to that of the Cor-OMePTPA/MAPbI₃ sample. A similar tendency was also observed in the mixed perovskite samples on different HTM films, as shown in Fig. S8. We speculated that a larger crystalline grain of perovskite will lead to a higher equality of the perovskite film, and this was demonstrated using X-ray diffraction (Fig. S9) and UV-Vis absorption (Fig. S10) measurements. Hence, we believed a better perovskite film obtained on the Cor-SMePTPA film would lead to fewer non-radiative recombination defects within the perovskite bulk phase, thereby increasing the photovoltaic performance and stability of the device. [19].

2.3. Charge transport ability of the HTM films

Hole extraction and transport are largely determined by the charge transport ability of the HTLs in a device. Subsequently, we evaluated the charge transport ability of the different HTM films using the space-charge-limited current (SCLC) method and photoluminescence (PL) measurements, as shown in Fig. 4. The measured current density–voltage (*J*-*V*) curves measured under dark conditions are shown in Fig. 4b and were used to calculate the hole mobility of different HTM films. The test device was set up as a hole-only device with an architecture of indium tin oxide (ITO)/poly(3, 4-ethylenedioxythiophene):poly(styrene-sulfonate) (PEDOT:PSS)/HTMs/MoO_x/Ag (Fig. 4a), [20] in which the PEDOT:PSS and HTM layers were fabricated via spin-coating and the MoO_x and Ag layers were deposited via thermal evaporation. The hole mobility of the materials was calculated according to the Mott-Gurney

equation as given below.

$$J = \frac{9\mu\epsilon_0\epsilon_r V^2}{8d^3} \quad (1)$$

where μ is the hole mobility, ϵ_0 represents the vacuum dielectric constant, ϵ_r stands for the relative dielectric constant, and d is determined by the film thickness. [21] The hole mobility increases from $1.16 \times 10^{-5} \text{ cm}^2 \text{ V}^{-1} \text{ s}^{-1}$ (Cor-OMePTPA) to $2.17 \times 10^{-5} \text{ cm}^2 \text{ V}^{-1} \text{ s}^{-1}$ (Cor-SMePTPA) upon substituting O atoms with S atoms. Increasing the hole mobility enhances the efficiency of the hole-transporting process, which could optimize the photovoltaic performance of the device.

Later on, we carried out PL measurements of different HTM/perovskite samples and the results are shown in Fig. 4c. According to the PL spectra, the perovskite film on the glass substrate exhibited a strong PL intensity, completely in keeping with a previous report. [15] Insertion of HTM films between the perovskites and glass substrates resulted in a dramatic reduction of the PL intensity. Furthermore, we observed a more considerable reduction in the PL intensity of the Cor-SMePTPA/perovskite, resulting from a more efficient hole-transporting process (Fig. 4b) and a better matched energy level of Cor-SMePTPA (Fig. 2d), as previously discussed. All the aforementioned results indicate that Cor-SMePTPA HTLs offer a higher PCE than Cor-OMePTPA HTLs, which inspired us to fabricate devices to test the performance of the material.

2.4. Photovoltaic performance and stability of the HTLs

To compare the device performance of the two HTLs, we initially selected an inverted PSC with a structure of FTO/corannulene-based HTLs/CH₃NH₃PbI₃/PCBM/BCP/Ag as the model device. We first optimized the thickness of the HTLs, which are largely determined by the

solution concentrations, and the results are listed in Table S2. We found that at an optimal HTM concentration of 2 mg mL^{-1} , a PCE of greater than 17% was obtained for the Cor-SMePTPA-based PSCs. By contrast, the Cor-OMePTPA-based PSCs only exhibited a modest PCE of 15.78%. Fig. 5a, S11 and S12 present the J - V curves of the champion devices, J - V curves varied with the concentration of HTM solutions and J - V curves under different scanning directions, respectively. To confirm the accuracy of the recorded photovoltaic parameters, we measured the external quantum efficiency (EQE) and steady-state output (SSO) measurements of the champion PSC, which are shown in Fig. 5b and 5c.

Then, we fabricated another inverted PSC based on an architecture of ITO/corannulene-based HTLs/mixed perovskite (FAMAPbCl)/ C_{60} /BCP/Ag to achieve improved photovoltaic performance, as displayed in Fig. 5d and S13. [22] Encouragingly, we obtained a maximum PCE of 21.70% with a V_{oc} of 1.12 V, a J_{sc} of 22.82 mA cm^{-2} , and an FF of 84.59% for the Cor-SMePTPA-based device. The EQE spectra, SSO measurement, J - V curves determined under different scanning directions and statistical PCE data of the champion Cor-SMePTPA-based device are shown in Fig. 5e, 5f, S14 and S15, respectively. Similar devices based on traditional NiO_x and PTAA HTLs were also fabricated for comparison, and the corresponding J - V curves and photovoltaic parameters are shown in Fig. S16.

By comprehensively analyzing the photovoltaic parameters of these two HTMs, it was observed that all photovoltaic parameters of the Cor-SMePTPA-based devices including V_{oc} , J_{sc} and FF were distinctly higher than those of the Cor-OMePTPA-based devices. In order to elucidate the underlying reason for the improved parameters, we thereby performed V_{oc} -light intensity tests and investigated the non-radiative/transport losses of different devices. First, the results shown in Fig. 5g mainly reflect the interfacial behavior in terms of carrier extraction and capture.

[23] The slopes of the fitted lines were determined using ideal factors (n_{ID}). The n_{ID} of the Cor-SMePTPA-based device (1.51) is smaller than that of the Cor-OMePTPA-based device (1.70), demonstrating optimal interfacial contact and suppression of non-radiative recombination at the HTL/perovskite interface, which contributes to deliver an optimized V_{oc} of the device. [24] Second, it was demonstrated that the Cor-SMePTPA exhibited a higher hole mobility than the Cor-OMePTPA (Fig. 4b). Generally, a higher mobility of the material leads to a better charge transporting process, which is expected to heighten the J_{sc} and FF of the devices. [17,20,25] To support this conclusion, we analyzed the contribution of different losses in the devices as shown in Fig. 5h. Thereinto, the FF S-Q limit is obtained from previous work, [26] the FF is the measured data of the devices, and the FF_{max} is calculated according to the following equation: [27]

$$FF_{max} = \frac{v_{oc} - \ln(v_{oc} + 0.72)}{v_{oc} + 1} \text{ with } v_{oc} = \frac{qV_{oc}}{n_{ID}k_B T} \quad (2)$$

Here, q is the elemental charge, k_B represents the Boltzmann constant, and T stands for the temperature. It's obvious that the Cor-SMePTPA-based device shows a lower non-radiative loss than the Cor-OMePTPA-based device, which is consistent with the n_{ID} analysis above (Fig. 5g). Furthermore, we found that the transport loss is dramatically reduced when replacing the Cor-OMePTPA HTL with the Cor-SMePTPA HTL, indicating a more efficient charge transporting process in the Cor-SMePTPA-based device, and thus resulting in a higher J_{sc} and FF of the device. [17,20].

Finally, the stability of the device under certain aging conditions cannot be neglected. We subjected the champion Cor-SMePTPA-based devices to environmental conditions (temperature of $\sim 20^\circ\text{C}$, and relative humidity in the 20%-30% range) without encapsulation and aged

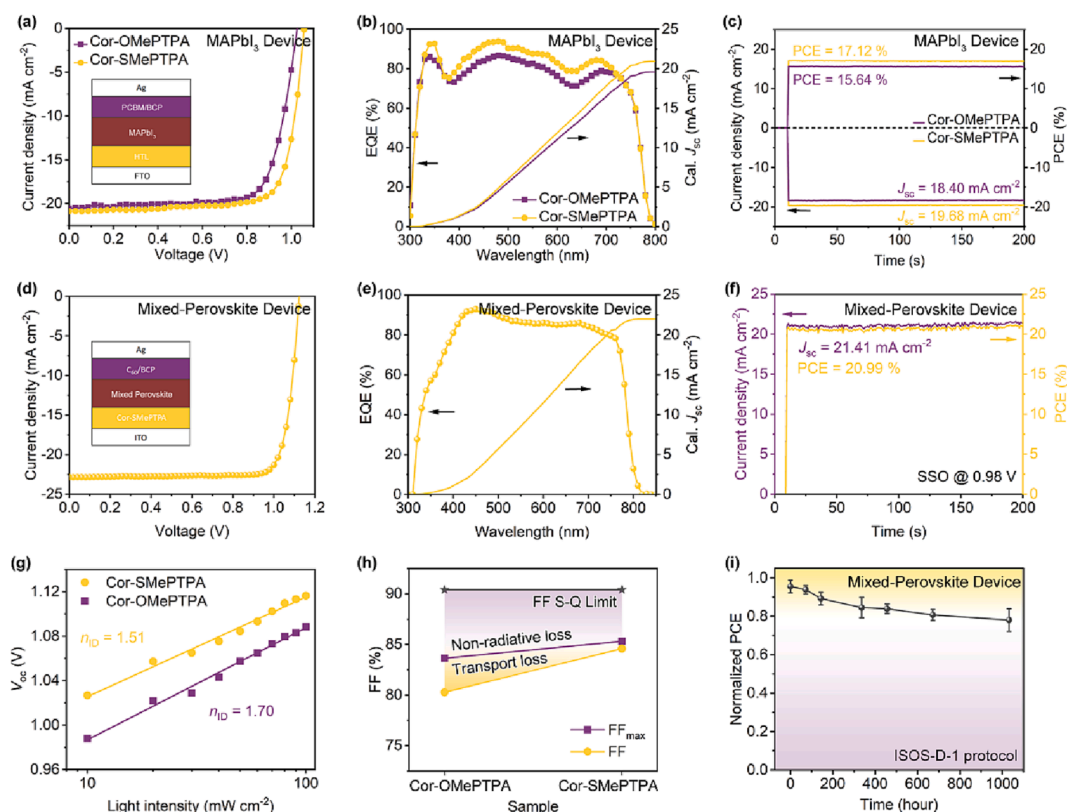


Fig. 5. (a) J - V curves, (b) EQE spectra and (c) SSO performance at maximum power point (0.85 V for Cor-OMePTPA and 0.87 V for Cor-SMePTPA) of different HTMs (2 mg mL^{-1})-based MAPbI_3 devices, respectively. (d) J - V curves, (e) EQE spectra and (f) SSO performance at maximum power point (0.98 V) of the Cor-SMePTPA-based mixed-perovskite device, respectively. (g) V_{oc} -light intensity measurements of different devices. (h) Analysis of non-radiative and transport losses in different devices. (i) The stability measurement of the champion Cor-SMePTPA-based mixed-perovskite device (temperature of $\sim 20^\circ\text{C}$, and relative humidity in 20%-30% range).

the devices according to the ISOS-D-1 protocol. [28] Fig. 5i revealed that the Cor-SMePTPA-based device possessed good stability with a T_{80} (80% of the initial PCE) lifetime of over 1000 h. The variations in the other parameters during the aging test are illustrated in Fig. S17. In summary, careful characterizations of the photovoltaic performance and stability of the devices led us to conclude that these star-like, dopant-free, corannulene-cored HTMs can be an ideal alternative for increasing the PCE and stability of inverted devices in the future.

3. Conclusion

In this study, we fabricated two star-like, dopant-free, corannulene-cored HTMs (Cor-OMePTPA and Cor-SMePTPA) into inverted PSCs for the first time. We obtained a maximum PCE of 21.70% for the champion Cor-SMePTPA-based PSC, which was among the highest PCE values of inverted devices containing SMe-terminated HTMs. This success was attributed to the extraordinary advantages of the corannulene core that were well matched with the specific requirements of HTLs for inverted PSCs. Furthermore, physical/chemical and photovoltaic measurements were performed to determine the effect of the underlying core and outer terminals (O or S) of the HTMs on the molecular characteristics, film properties, and device performance and stability. We expect that these corannulene-cored HTMs can be further upgraded to bring new life into the design of novel HTMs for obtaining high-performance and stable PSCs.

4. Experimental section

4.1. Materials

All reagents were purchased from Alfa-Aesar, J&K, Sigma-Aldrich, or other commercial suppliers. All reactions dealing with air- or moisture-sensitive compounds were carried out using standard Schlenk techniques. *sym*-penta(*N*, *N*-bis(4-methoxyphenyl)aniline) corannulene (denoted as **Cor-OMePTPA**) was synthesized according to our previous work. [9] 1, 3, 5, 7, 9-pentakis(Bpin)corannulene (denoted as **R1**) and 4-bromo-*N*, *N*-bis(4-(methylthio)phenyl)aniline (denoted as **Br-SMeTPA**) were synthesized according to previous literatures. [29,30] The FTO and ITO glasses were purchased from Advanced Election Technology Co., Ltd. Perovskite raw materials and BCP were obtained from Xi'an Polymer Light Technology Corp. C₆₀ was obtained from Puyang Yongxin Fullerene Co., Ltd.

4.2. Synthetic procedures

sym-penta(*N*, *N*-bis(4-(methylthio)phenyl)aniline) corannulene (denoted as **Cor-SMePTPA**) was synthesized as shown in Fig. S2. A mixture of **R1** (270 mg, 0.307 mmol), **Br-SMeTPA** (1.27 g, 3.07 mmol), Pd(PPh₃)₄ (88.98 mg, 0.077 mmol), and Cs₂CO₃ (3.0 g, 9.21 mmol) in a Schlenk flask was then added DMF (150 mL) under argon atmosphere. The mixture was heated to 80 °C for 24 h. After removal of the solvent, the crude product was purified via column chromatography (silica gel) using CH₂Cl₂/ethyl acetate (50:1) as eluent to give compound **Cor-SMePTPA** as a bright yellow solid (220 mg, 37.2%). ¹H NMR (CDCl₃, 500 MHz, δ/ppm): 7.88 (s, 1H), 7.58 (d, *J* = 8 Hz, 2H), 7.22 (d, *J* = 8.5 Hz, 4H), 7.15 (d, *J* = 8 Hz 2H), 7.11 (d, *J* = 7.5 Hz, 4H), 2.49 (s, 6H). ¹³C NMR (CDCl₃, 125 MHz, δ/ppm): 146.87, 144.65, 141.48, 135.13, 133.49, 132.43, 130.50, 128.99, 128.35, 125.51, 122.50, 16.56. Mass found: *m/z* 1926.885 [M⁺]; Calcd. C₁₂₀H₉₅N₅S₁₀: *m/z* 1926.482.

4.3. Device fabrication

Patterned FTO and ITO glasses were cleaned by using an ultrasonic bath with detergent, deionized water, acetone and isopropanol (IPA) for 10 min, and then dried by N₂ gas. The glasses were UVO-treated for 10 min before fabricated the HTLs. Different concentrations of HTM

toluene solutions were spin-coated at 3000 rpm for 30 s and annealed at 100 °C for 20 min. After cooling down to room temperature, different perovskite films were fabricated according to our previous works. [15,22] Briefly, as for the MAPbI₃ perovskite, 1.4 M precursor solution (in DMF) containing MAI and PbI₂ was spin-coated at 4000 rpm for 30 s, and quickly dripped down 500 μL isopropyl ether as the anti-solvent within the first 10 s. As for the mixed perovskite, 34.4 mg FAI, 174.9 mg MAI, 539.37 mg PbI₂ and 36.2 mg PbCl₂ were completely dissolved in DMF:DMSO = 8:1. Then, the precursor solution was spin-coated at 1000 rpm for 10 s and 4000 rpm for 28 s, and 150 μL ethyl acetate was dropped onto the film at 21 s before the end. All the substrates were then annealed at 100 °C for 10 min to enhance the perovskite crystallinity. Later on, PCBM ETLs were fabricated by spin-coating PCBM chlorobenzene solutions at 3000 rpm for 20 s, while C₆₀ ETLs were thermally evaporated for a thickness about 40 nm. Subsequently, 0.5 mg mL⁻¹ BCP IPA solutions were spin-coated above the ETLs at 6000 rpm for 30 s, and annealed at 80 °C for 10 min. Finally, Ag electrodes were thermally evaporated for 100 nm at 2.0 × 10⁻⁴ Pa to finish the device fabrication.

4.4. Characterizations

¹H NMR and ¹³C NMR spectra were recorded by using Bruker Biospin AvanceIII 500 MHz spectrometers. TGA curve was recorded on a SDT 600 instrument under a N₂ flux of 100 mL min⁻¹ and a heating rate of 10 °C min⁻¹. UV-Vis absorption spectra were obtained by using a Jasco-V-780 ultraviolet spectrophotometer. Transmittance spectra were obtained on a Cary-5000 UV-Vis-NIR spectrophotometer. PL spectra were recorded on a Hitachi F7000 fluorescence spectrophotometer. CV analysis were conducted by using a Shanghai Chenhua CHI-660C electrochemical station. The detail methods were listed as follow: 0.1 M Bu₄NPF₆ CH₂Cl₂ electrolyte, N₂ atmosphere, 25 °C, 100 mV s⁻¹. The top and cross-sectional view SEM images were obtained through a HITACHI S-4800 scanning electron microscope. Photovoltaic parameters of PSCs were recorded by using a Keithley 2400 source meter under AM 1.5G 100 mW cm⁻² illumination. The active area was calibrated through an aperture of 0.037 cm². The champion PCE was measured at the following conditions: 1.2 V to -0.2 V with a scanning speed of 0.02 V s⁻¹. EQE curves were obtained through a Newport EQE system. SSO measurements were performed on a Shanghai Chenhua CHI-650E electrochemical station. Water contact angle tests were carried out by using a SDC-100 contact angle analyzer. DFT calculations were performed on Gaussian 16 program with B3LYP function and 6-31G(d) basis set in the gas phase. [31] The XPS and UPS measurements were conducted on a Thermo Escalab 250XI equipment. The XRD measurements were carried out by using a Rigaku Ultima IV equipment.

Declaration of Competing Interest

The authors declare the following financial interests/personal relationships which may be considered as potential competing interests: Ming-Wei An, Lin-Long Deng has patent licensed to Xiamen University.

Data availability

Data will be made available on request.

Acknowledgements

We thank the National Natural Science Foundation of China (52203228, 92061122), the China Postdoctoral Science Foundation (2022M711464) and Natural Science Foundation of Guangdong Province of China (2023A1515011916). We also thank the Start-up funding from Fujian Normal University and Prof. Qianyan Zhang from Xiamen University for his kind assistances in material and discussion.

Appendix A. Supplementary data

Supplementary data to this article can be found online at <https://doi.org/10.1016/j.cej.2023.144056>.

References

- Q. Jiang, J. Tong, Y. Xian, R.A. Kerner, S.P. Dunfield, C. Xiao, R.A. Scheidt, D. Kuciauskas, X. Wang, M.P. Hautzinger, R. Tirawat, M.C. Beard, D.P. Penning, J. J. Berry, B.W. Larson, Y. Yan, K. Zhu, Surface Reaction for Efficient and Stable Inverted Perovskite Solar Cells, *Nature* 611 (7935) (2022) 278–283, <https://doi.org/10.1038/s41586-022-05268-x>.
- Z. Xing, S.-H. Li, S. Yang, Targeted Molecular Design of Functionalized Fullerenes for High-Performance and Stable Perovskite Solar Cells, *Small Struct.* 3 (6) (2022) 2200012, <https://doi.org/10.1002/sstr.202200012>.
- Y. Yao, C. Cheng, C. Zhang, H. Hu, K. Wang, S. De Wolf, Organic Hole-Transport Layers for Efficient, Stable, and Scalable Inverted Perovskite Solar Cells, *Adv. Mater.* 34 (44) (2022) 2203794, <https://doi.org/10.1002/adma.202203794>.
- N. Tiwari, H. Arianita Dewi, E. Erdenebileg, R. Narayan Chauhan, N. Mathews, S. Mhaisalkar, A. Bruno, Advances and Potentials of NiO_x Surface Treatments for *p*-*i*-*n* Perovskite Solar Cells, *Sol. RRL* 6 (3) (2022) 2100700, <https://doi.org/10.1002/solr.202100700>.
- C.C. Boyd, R.C. Shallick, T. Moot, R. Kerner, L. Bertoluzzi, A. Onno, S. Kavadiya, C. Chosy, E.J. Wolf, J. Werner, J.A. Raiford, C. de Paula, A.F. Palmstrom, Z.J. Yu, J. J. Berry, S.F. Bent, Z.C. Holman, J.M. Luther, E.L. Ratcliff, N.R. Armstrong, M. D. McGehee, Overcoming Redox Reactions at Perovskite-Nickel Oxide Interfaces to Boost Voltages in Perovskite Solar Cells, *Joule* 4 (8) (2020) 1759–1775, <https://doi.org/10.1016/j.joule.2020.06.004>.
- Y. Wang, L. Duan, M. Zhang, Z.-C. Chen, Y. Su, L.-L. Deng, S.-H. Li, Z.-A. Nan, H.-R. Tian, X.-L. Liu, D.-Q. Yun, Q. Zhang, S.-Y. Xie, L.-S. Zheng, Corannulene-Based Hole-Transporting Material for Efficient and Stable Perovskite Solar Cells, *Cell Rep. Phys. Sci.* 2 (12) (2021), 100662, <https://doi.org/10.1016/j.xcrp.2021.100662>.
- Z. Xing, M.-W. An, Z.-C. Chen, M. Hu, X. Huang, L.-L. Deng, Q. Zhang, X. Guo, S.-Y. Xie, S. Yang, Surface Re-Engineering of Perovskites with Buckybowls to Boost the Inverted-Type Photovoltaics, *J. Am. Chem. Soc.* 144 (30) (2022) 13839–13850, <https://doi.org/10.1021/jacs.2c05235>.
- Z. Xing, F. Liu, S.-H. Li, Z.-C. Chen, M.-W. An, S. Zheng, A.K.Y. Jen, S. Yang, Multifunctional Molecular Design of a New Fulleropyrrolidine Electron Transport Material Family Engenders High Performance of Perovskite Solar Cells, *Adv. Funct. Mater.* 31 (51) (2021) 2107695, <https://doi.org/10.1002/adfm.202107695>.
- Q. Zhuang, C. Zhang, C. Gong, H. Li, H. Li, Z. Zhang, H. Yang, J. Chen, Z. Zhang, Tailoring Multifunctional Anion Modifiers to Modulate Interfacial Chemical Interactions for Efficient and Stable Perovskite Solar Cells, *Nano Energy* 102 (2022), 107747, <https://doi.org/10.1016/j.nanoen.2022.107747>.
- C. Gong, C. Zhang, Q. Zhuang, H. Li, H. Yang, J. Chen, Z. Zhang, Stabilizing Buried Interface via Synergistic Effect of Fluorine and Sulfonyl Functional Groups Toward Efficient and Stable Perovskite Solar Cells, *Nano-Micro Lett.* 15 (1) (2022) 17, <https://doi.org/10.1007/s40820-022-00992-5>.
- Y. Lin, L. Shen, J. Dai, Y. Deng, Y. Wu, Y. Bai, X. Zheng, J. Wang, Y. Fang, H. Wei, W. Ma, X.C. Zeng, X. Zhan, J. Huang, π -Conjugated Lewis Base: Efficient Trap-Passivation and Charge-Extraction for Hybrid Perovskite Solar Cells, *Adv. Mater.* 29 (7) (2017) 1604545, <https://doi.org/10.1002/adma.201604545>.
- Z. Xing, S.-H. Li, Y. Hui, B.-S. Wu, Z.-C. Chen, D.-Q. Yun, L.-L. Deng, M.-L. Zhang, B.-W. Mao, S.-Y. Xie, R.-B. Huang, L.-S. Zheng, Star-Like Hexakis[di(ethoxycarbonyl)methano]-C₆₀ with Higher Electron Mobility: An Unexpected Electron Extractor Interfaced in Photovoltaic Perovskites, *Nano Energy* 74 (2020), 104859, <https://doi.org/10.1016/j.nanoen.2020.104859>.
- W. Zhao, D. Qian, S. Zhang, S. Li, O. Inganäs, F. Gao, J. Hou, Fullerene-Free Polymer Solar Cells with over 11% Efficiency and Excellent Thermal Stability, *Adv. Mater.* 28 (23) (2016) 4734–4739, <https://doi.org/10.1002/adma.201600281>.
- Y. Wang, Q. Liao, J. Chen, W. Huang, X. Zhuang, Y. Tang, B. Li, X. Yao, X. Feng, X. Zhang, M. Su, Z. He, T.J. Marks, A. Facchetti, X. Guo, Teaching an Old Anchoring Group New Tricks: Enabling Low-Cost, Eco-Friendly Hole-Transporting Materials for Efficient and Stable Perovskite Solar Cells, *J. Am. Chem. Soc.* 142 (39) (2020) 16632–16643, <https://doi.org/10.1021/jacs.0c06373>.
- M. Wang, H. Wang, W. Li, X. Hu, K. Sun, Z. Zang, Defect Passivation Using Ultrathin PTAA Layers for Efficient and Stable Perovskite Solar Cells with a High Fill Factor and Eliminated Hysteresis, *J. Mater. Chem. A* 7 (46) (2019) 26421–26428, <https://doi.org/10.1039/C9TA08314F>.
- Y. Hui, Y.-Y. Tan, L. Chen, Z.-A. Nan, J.-Z. Zhou, J.-W. Yan, B.-W. Mao, Stability of Perovskite Thin Films under Working Condition: Bias-Dependent Degradation and Grain Boundary Effects, *Adv. Funct. Mater.* 31 (36) (2021) 2103894, <https://doi.org/10.1002/adfm.202103894>.
- Y. Wang, W. Chen, L. Wang, B. Tu, T. Chen, B. Liu, K. Yang, C.W. Koh, X. Zhang, H. Sun, G. Chen, X. Feng, H.Y. Woo, A.B. Djurišić, Z. He, X. Guo, Dopant-Free Small-Molecule Hole-Transporting Material for Inverted Perovskite Solar Cells with Efficiency Exceeding 21%, *Adv. Mater.* 31 (35) (2019) 1902781, <https://doi.org/10.1002/adma.201902781>.
- P.N. Murgatroyd, Theory of Space-Charge-Limited Current Enhanced by Frenkel Effect, *J. Phys. D: Appl. Phys.* 3 (2) (1970) 151–156, <https://doi.org/10.1088/0022-3727/3/2/308>.
- W. Kong, W. Li, C. Liu, H. Liu, J. Miao, W. Wang, S. Chen, M. Hu, D. Li, A. Amini, S. Yang, J. Wang, B. Xu, C. Cheng, Organic Monomolecular Layers Enable Energy-Level Matching for Efficient Hole Transporting Layer Free Inverted Perovskite Solar Cells, *ACS Nano* 13 (2) (2019) 1625–1634, <https://doi.org/10.1021/acsnano.8b07627>.
- P. Caprioglio, M. Stollerfoht, C.M. Wolff, T. Unold, B. Rech, S. Albrecht, D. Neher, On the Relation between the Open-Circuit Voltage and Quasi-Fermi Level Splitting in Efficient Perovskite Solar Cells, *Adv. Energy Mater.* 9 (33) (2019) 1901631, <https://doi.org/10.1002/aenm.201901631>.
- C. Zhang, H. Wang, H. Li, Q. Zhuang, C. Gong, X. Hu, W. Cai, S. Zhao, J. Chen, Z. Zang, Simultaneous Passivation of Bulk and Interface Defects through Synergistic Effect of Anion and Cation Toward Efficient and Stable Planar Perovskite Solar Cells, *J. Energy Chem.* 63 (2021) 452–460, <https://doi.org/10.1016/j.jechem.2021.07.011>.
- K. Chen, Q. Hu, T. Liu, L. Zhao, D. Luo, J. Wu, Y. Zhang, W. Zhang, F. Liu, T. P. Russell, R. Zhu, Q. Gong, Charge-Carrier Balance for Highly Efficient Inverted Planar Heterojunction Perovskite Solar Cells, *Adv. Mater.* 28 (48) (2016) 10718–10724, <https://doi.org/10.1002/adma.201604048>.
- M. Stollerfoht, C.M. Wolff, Y. Amir, A. Paulke, L. Perdigon-Toro, P. Caprioglio, D. Neher, Approaching the Fill Factor Shockley-Queisser Limit in Stable, Dopant-Free Triple Cation Perovskite Solar Cells, *Cells* 10 (6) (2017) 1530–1539, <https://doi.org/10.1039/C7EE00899F>.
- Q. Cao, Y. Li, H. Zhang, J. Yang, J. Han, T. Xu, S. Wang, Z. Wang, B. Gao, J. Zhao, X. Li, X. Ma, S.M. Zakeeruddin, W.E.I. Sha, X. Li, M. Grätzel, Efficient and Stable Inverted Perovskite Solar Cells with Very High Fill Factors via Incorporation of Star-Shaped Polymer, *Sci. Adv.* 7 (28) (2021), eabg0633, <https://doi.org/10.1126/sciadv.abg0633>.
- M.V. Khenkin, E.A. Katz, A. Abate, G. Bardizza, J.J. Berry, C. Brabec, F. Brunetti, V. Bulović, K. Burlingame, A. Di Carlo, R. Cheacharon, Y.-B. Cheng, A. Colmann, S. Cros, K. Domanski, M. Duszka, C.J. Fell, S.R. Forrest, Y. Galagan, D. Di Girolamo, M. Grätzel, A. Hagfeldt, E. von Hauff, H. Hoppe, J. Kettle, H. Köbler, M.S. Leite, S. Liu, Y.-L. Loo, J.M. Luther, C.-Q. Ma, M. Madsen, M. Manceau, M. Matheron, M. McGehee, R. Meitzner, M.K. Nazeeruddin, A.F. Nogueira, C. Odabasi, A. Osherov, N.-G. Park, M.O. Reese, F. De Rossi, M. Saliba, U.S. Schubert, H. J. Snaith, S.D. Stranks, W. Tress, P.A. Troshin, V. Turkevich, S. Veenstra, I. Visoly-Fisher, A. Walsh, T. Watson, H. Xie, R. Yıldırım, S.M. Zakeeruddin, K. Zhu, M. Lira-Cantu, Consensus Statement for Stability Assessment and Reporting for Perovskite Photovoltaics Based on ISOS Procedures, *Nat. Energy* 5 (1) (2020) 35–49, <https://doi.org/10.1038/s41560-019-0529-5>.
- M. Planells, A. Abate, D.J. Hollman, S.D. Stranks, V. Bharti, J. Gaur, D. Mohanty, S. Chand, H.J. Snaith, N. Robertson, Diacetylene Bridged Triphenylamines as Hole Transport Materials for Solid State Dye Sensitized Solar Cells, *J. Mater. Chem. A* 1 (23) (2013) 6949–6960, <https://doi.org/10.1039/C3TA11417A>.
- Z.-Z. Zhu, Z.-C. Chen, Y.-R. Yao, C.-H. Cui, S.-H. Li, X.-J. Zhao, Q. Zhang, H.-R. Tian, P.-Y. Xu, F.-F. Xie, X.-M. Xie, Y.-Z. Tan, S.-L. Deng, J.M. Quimby, L.T. Scott, S.-Y. Xie, R.-B. Huang, L.-S. Zheng, Rational Synthesis of An Atomically Precise Carboncone under Mild Conditions, *Sci. Adv.* 5 (8) (2019), eaaw0982, <https://doi.org/10.1126/sciadv.aaw0982>.
- M. J. Frisch, G. W. Trucks, H. B. Schlegel, G. E. Scuseria, M. A. Robb, J. R. Cheeseman, G. Scalmani, V. Barone, G. A. Petersson, H. Nakatsuji, X. Li, M. Caricato, A. Marenich, J. Bloino, B. G. Janesko, R. Gomperts, B. Mennucci, H. P. Hratchian, J. V. Ortiz, A. F. Izmaylov, J. L. Sonnenberg, D. Williams-Young, F. Ding, F. Lipparini, F. Egidi, J. Goings, B. Peng, A. Petrone, T. Henderson, D. Ranasinghe, V. G. Zakrzewski, J. Gao, N. Rega, G. Zheng, W. Liang, M. Hada, M. Ehara, K. Toyota, R. Fukuda, J. Hasegawa, M. Ishida, T. Nakajima, Y. Honda, O. Kitao, H. Nakai, T. Vreven, K. Throssell, J. A. Montgomery, Jr., J. E. Peralta, F. Ogliaro, M. Bearpark, J. J. Heyd, E. Brothers, K. N. Kudin, V. N. Staroverov, T. Keith, R. Kobayashi, J. Normand, K. Raghavachari, A. Rendell, J. C. Burant, S. S. Iyengar, J. Tomasi, M. Cossi, J. M. Millam, M. Klene, C. Adamo, R. Cammi, J. W. Ochterski, R. L. Martin, K. Morokuma, O. Farkas, J. B. Foresman, D. J. Fox, Gaussian 16 Revision A.03, Gaussian Inc. Wallingford CT (2016).